Complete characterization of sub-Coulomb-barrier tunneling with phase-of-phase attoclock

Meng Han[1,2], Peipei Ge[1], Jiguo Wang[1], Zhenning Guo[1], Yiqi Fang[1], Xueyan Ma[1], Xiaoyang Yu[1], Yongkai Deng[1], Hans Jakob Wörner[2], Qihuang Gong[1,3,4,5,6], and Yunquan Liu[1,3,4,5,6,*]

[1]State Key Laboratory for Mesoscopic Physics and and Frontiers Science Center for Nano-optoelectronics, School of Physics, Peking University, Beijing, 100871, China

[2]Laboratorium für Physikalische Chemie, ETH Zürich, Zürich, 8093, Switzerland

[3]Collaborative Innovation Center of Quantum Matter, Beijing, 100871, China

[4]Collaborative Innovation Center of Extreme Optics, Shanxi University, Taiyuan, 030006, China

[5]Peking University Yangtze Delta Institute of Optoelectronics, Nantong, Jiangsu, 226010, China

[6]Beijing Academy of Quantum Information Sciences, Beijing, 100193, China

[*]yunquan.liu@pku.edu.cn

ABSTRACT

Laser-induced electron tunneling, triggering a broad range of ultrafast phenomena such as the generation of attosecond light pulses, photoelectron diffraction and holography, has laid the foundation of strong-field physics and attosecond science. Using the attoclock constructed by single-color elliptically polarized laser fields, previous experiments have measured the tunneling rates, exit positions, exit velocities and delay times for some specific electron trajectories, which are mostly born at the field peak instant where the laser electric field and the formed potential barrier are stationary in terms of the derivative versus time. From the view of the wave-particle dualism, the electron phase under a classically forbidden, tunneling barrier has not been measured, which is at the heart of quantum tunneling physics. Here we present a robust measurement of tunneling dynamics including the electron sub-barrier phase and amplitude. We combine attoclock technique with two-color phase-of-the-phase spectroscopy to accurately calibrate the angular streaking relation and to probe the non-stationary tunneling dynamics by manipulating a rapidly changing potential barrier. This phase-of-phase attoclock (POP attoclock) directly links the measured phase of the two-color relative phase with the ionization instant for the photoelectron with any final momentum on the “detector”, which allows us to reconstruct the imaginary tunneling time and the accumulated phase under the barrier. The POP attoclock provides a general time-resolved approach to access the underlying quantum dynamics in intense-light-matter interactions.

The tunneling of a micro-particle through a barrier is one of the most fundamental and ubiquitous quantum processes. In strong-field ionization the oscillating electric field of laser pulses creates a time-dependent potential barrier in atoms or molecules allowing the bound electron to tunnel. At the instant of the field peak the potential barrier is the thinnest and stationary as the derivative versus time is zero. After the peak instant, the potential barrier changes quickly on the attosecond timescale, still triggering a series of tunneling bursts or electrons with different probabilities at different positions. This sub-cycle electron dynamics greatly enriches strong-field phenomena[1], ranging from strong-field ionization to high-order harmonic emission. Previous measurements mainly focus on the most probable tunneling burst which is born at the instant of the field peak, such as the efforts on the tunneling time delay[2–11], exit velocities[12–14] and exit positions[15–17]. In contrast, the tunneling dynamics under a classically forbidden, non-stationary barrier is less explored, especially for the electron sub-barrier phase, which is essential to fully understand and characterize this fundamental quantum mechanical process.

The sub-cycle tunneling bursts could be mapped to different emitting angles within elliptically or circularly polarized light fields, which is the principle of the attoclock[2,3]. There, the mapping relation between the final photoelectron momentum $\boldsymbol{p}$ and its ionization instant t relies on an important, but unproved assumption that the angle-time mapping is angularly uniform. For the photoelectron with the maximum yield in the final momentum space, it is clear that it originates from the tunneling burst born at the instant of the electric-field peak. However, as for the photoelectron with a general momentum (e.g., see the red box in Figure 1a), actually one cannot determine its ionization instant without the assumption of the uniform mapping. Indeed, as we shown in this work, this assumption is not valid (i.e., the rotation angle of the electric field vector β_ω is not identical to that of the electron momentum vector α_p in Figure 1a). To realize the time-resolved ability in the full momentum space, determining the ionization instant of each non-stationary tunneling burst and probing its sub-Coulomb barrier dynamics become the key challenges in ultrafast science.

Recently, the phase-of-phase photoelectron spectroscopy was introduced to extract the scattering structural information of atoms, molecules and nanoparticles[18–23], in which the momentum-resolved electron yield is Fourier transformed with respect to the relative phase between two-color laser fields to obtain the phase of the yield oscillation, which is the so-called phase of the phase. The phase-of-phase spectrum provides rich dynamical information than the static photoelectron spectra measured in the one-color field. However, the physical meaning of the obtained phase of the phase is not straightforward and thus the application of this elegant time-resolved photoelectron spectroscopy is limited.

Here we introduce phase-of-phase attoclock (POP attoclock) spectroscopy, i.e., combining the attoclock and

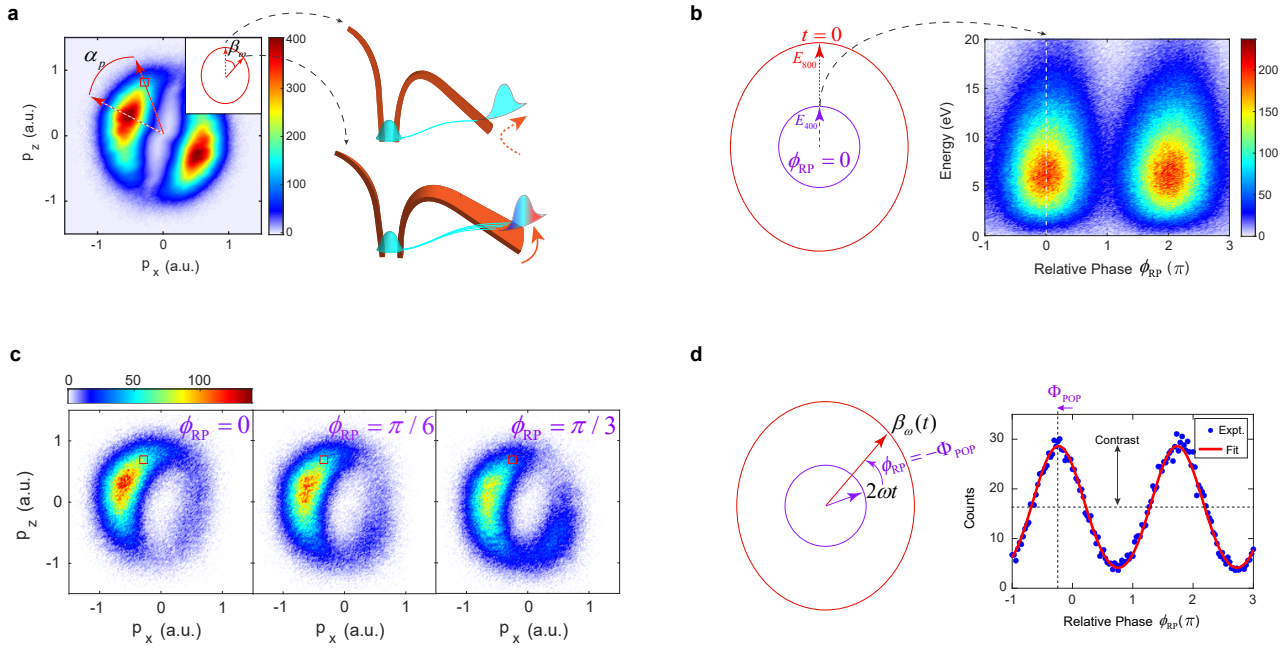

Figure 1: **Phase-of-phase attoclock photoelectron spectroscopy**. **a**, Measured photoelectron momentum distribution in a common attoclock configuration, in which a strong elliptically polarized 800-nm fundamental wave (FW, indicated by a red ellipse in the inset) is used to trigger a series of tunneling bursts following the rotating electric-field vector. The red dashed arrow and the red solid arrow identify the static tunneling at the field crest and the non-stationary tunneling in the falling edge, respectively. At the two ionization instants, the change tendency of the potential barrier is different, which is indicated by the crooked orange arrows near the barrier. Different sub-barrier dynamics gives rise to the different phase distribution on the emitting electron wave-packet (indicated by the color). **b**, Calibration of the relative phase in the POP attoclock configuration, in which a weak co-rotating circularly polarized second harmonic (SH) field is added into the common attoclock. The left panel shows the defined zero point for the relative phase, where the two fields both point to the vertical upward direction at the ionization instant of $t = 0$ so that the barrier will be bent to the maximum extent and its corresponding electron lobe in the final momentum plane (i.e., the left lobe) will reach the yield maximum. The right panel shows measured photoelectron energy spectrum for the left electron lobe as a function of the relative phase between two fields, from which we can accurately calibrate the relative phase between two fields. Here the emitting angle $\theta = \mathrm{atan}(p_z/p_x)$ was integrated from 70° to 250°. **c**, Measured photoelectron momentum distributions at the relative phases of 0, $\pi/6$, $\pi/3$. **d**, Measured phase-resolved electron yield (blue dots) for a given photoelectron momentum [(p_x, p_z) = (-0.2, 0.74) a.u., indicated by the red boxes in a and c] and the fit curve by $A + P\cos(\phi_{RP} + \Phi_{POP})$ (red curve). Two characteristic parameters of the yield oscillation, the contrast P and the phase of the phase Φ_{POP}, are indicated in the plot. Since the direction of the SH clock hand is determined by $2\omega t + \phi_{RP}$, tuning the relative phase ϕ_{RP} (equivalent to rotating the clock hand) can build a mapping relation between the direction of the FW clock hand, $\beta_\omega(t)$, with the phase of the phase, Φ_{POP}, as illustrated in the left panel of d. When the ϕ_{RP} is tuned to be $-\Phi_{POP}$, the two clock hands are parallel and the ionization probability is the maximum.

the phase-of-phase spectroscopy, to resolve the ionization instant of photoelectrons with any momenta on the "detector" and further reconstruct the imaginary tunneling time and the sub-barrier phase acquired in the non-stationary tunneling process. A strong elliptically polarized fundamental wave (FW) is used to trigger the dynamical sub-cycle tunneling bursts, and a weak co-rotating circularly polarized second harmonic (SH) serves to perturb the potential barrier uniformly and to probe the time-dependent tunneling dynamics by adjusting the two-color relative phase. The synthesized electric field can be expressed as $E(t) = [E_\omega \cos(\omega t) + E_{2\omega} \cos(2\omega t + \phi_{RP})]\hat{z} + [\varepsilon E_\omega \sin(\omega t) + E_{2\omega} \sin(2\omega t + \phi_{RP})]\hat{x}$, where $\varepsilon = 0.80$ is the ellipticity of the FW. The relative phase between the two-color fields ϕ_{RP} was continuously controlled by a pair of fused silica wedges mounted on the piezo-driven motors. The peak intensity of the fundamental field is 1.0×10^{14} W/cm^2 ($E_\omega = 0.04$ a.u.; a.u. is atomic unit) and that of the second harmonic was controlled at a very low level about 1.0×10^{12} W/cm^2 ($E_{2\omega} = 0.004$ a.u.). We measured the photoelectron momentum distribution of single ionization from krypton atoms using cold-target recoil-ion reaction momentum spectroscopy (COLTRIMS)[24,25].

In the fundamental field solely, the photoelectron momentum distribution reveals two lobes, as illustrated in Fig. 1a, which can be understood by angular streaking by elliptically polarized fields (attoclock). The main lobes originate from strong-field tunneling ionization around the two field crests of one optical cycle. The emitting angle of the lobe center deviates from the direction of the laser vector potential at the peak instant, i.e., the x axis. The offset angle is caused by the Coulomb rotation in the continuum[4,5], while it could be related with the tunneling time delay and exit velocities[6–11]. For all previous attoclock experiments, the offset angle was determined only for the momentum with the maximum yield, and then the angle-to-time mapping was assumed to be isotropic according to the semi-classical model. However, as discussed in this work, for the photoelectron with a general momentum in the final momentum plane, its offset angle is not simply identical to that with the maximum yield since its sub-barrier dynamics is different and its ionization instant will be modified accordingly. Therefore, the construction of the mapping relation between an arbitrary $\boldsymbol{p}$ and t is the critical step to fully characterize the sub-barrier non-stationary tunneling dynamics.

In the geometry of POP attoclock, there are two temporal degrees of freedom, i.e., the ionization instant t and the two-color relative phase ϕ_{RP}. The direction of the FW clock hand is uniquely determined by the ionization instant and that of the SH clock hand depends on the two variables. The ionization instant is intrinsic, and we use the externally controllable relative phase to measure the ionization instant. Note that here the calibration of the relative phase does not rely on any theoretical models. At $\phi_{\mathrm{RP}} = 0$, the two clock hands both point to the positive direction of z axis at $t = 0$ (see Figure 1b) and they will be oriented opposite along the z axis at the other peak instant $t = \pi/\omega$.

Thus, at $\phi_{RP} = 0$ the left upper electron lobe in the final momentum plane, which corresponds to the peak instant of $t = 0$, should reach the yield maximum and the right lower lobe should achieve the yield minimum. In Figure 1b, we illustrate the angle-integrated energy spectrum for the left upper electron lobe as a function of the relative phase, from which the phase calibration can be performed accurately. After the phase calibration, we illustrate the photoelectron momentum distributions in the two-color fields at the relative phase of zero, $\pi/6$ and $\pi/3$ in Figure 1c. With the increase of ϕ_{RP}, the centroid of the momentum distribution gradually rotates counterclockwise. In Supplementary Section 3, we illustrate the complete phase-resolved movie of the photoelectron angular distribution. For each momentum [see the example of (p_x, p_z, p_y) = (-0.2, 0.74, 0) a.u. in Figure 1d], the yield oscillation with respect to the relative phase is close to a standard cosine function $A + P\cos(\phi_{RP} + \Phi_{POP})$, where A is the background count, P is the contrast, and Φ_{POP} is the so-called phase of the phase[18] ranging from $-\pi$ to π. Mathematically, the value of Φ_{POP} represents the waiting time ($\Phi_{POP} < 0$) or the passed time ($\Phi_{POP} > 0$) of the appearing instant of the yield peak with respect to the instant of $\phi_{RP} = 0$ during the yield oscillation. However, a clear physical meaning of Φ_{POP} is not identified in previous phase-of-phase experiments[18–23].

In the phase-of-phase spectroscopy, re-scattering and sub-cycle interference cause the difficulty to dig the deeper physical meaning of the phase of the phase. Here we show it is directly corresponding to the photoelectron ionization instant in this POP attoclock configuration. The photoelectron yield Y at the momentum $\boldsymbol{p}$ exponentially depends on the strength of the synthesized electric field $|E(t)|$ at its ionization instant t. In the POP attoclock, $|E(t)|$ can be reduced to $F_\omega(t) + E_{2\omega}\cos(2\omega t - \beta_\omega + \phi_{RP})$, saving to the first order of the small quantity $E_{2\omega}/E_\omega$, where $F_\omega(t)$ is the strength of the FW clock hand and $\beta_\omega(t)$ is its orientation angle. Then, one can obtain the momentum- and phase-resolved yield $Y(\boldsymbol{p}, \phi_{RP}) \sim \exp[|E(t)|] \sim Y_0(\boldsymbol{p})[1 + E_{2\omega}\cos(2\omega t - \beta_\omega + \phi_{RP})]$ (see Supplementary Section 2 for the mathematical derivation), where $Y_0(\boldsymbol{p}) \sim \exp[\beta_\omega(\mathrm{t})]$ is the yield without adding the perturbative field. Thus, the phase of the yield oscillation with respect to ϕ_{RP} is $\Phi_{POP} = 2\omega t - \beta_\omega(t)$, while the contrast of the yield oscillation is $Y_0(\boldsymbol{p})E_{2\omega}$. For the FW field with high ellipticity, there is $\beta_\omega \approx \omega t$. Finally, the phase of the phase is directly linked with the ionization instant, i.e., $\Phi_{POP} = \omega t$.

The principle of the POP attoclock can be understood intuitively. As illustrated in Figure 1d, varying the relative phase is equivalent to rotating the SH clock hand. When the SH clock hand points to the same direction of the FW clock hand, the photoelectron yield will achieve the maximum and thus this instant is marked. Because the scale of the SH clock has been calibrated, one can use it to measure the direction of the FW clock hand, i.e., the ionization instant.

The experimental phase-of-phase spectrum and the contrast spectrum for krypton atoms are presented in Figure

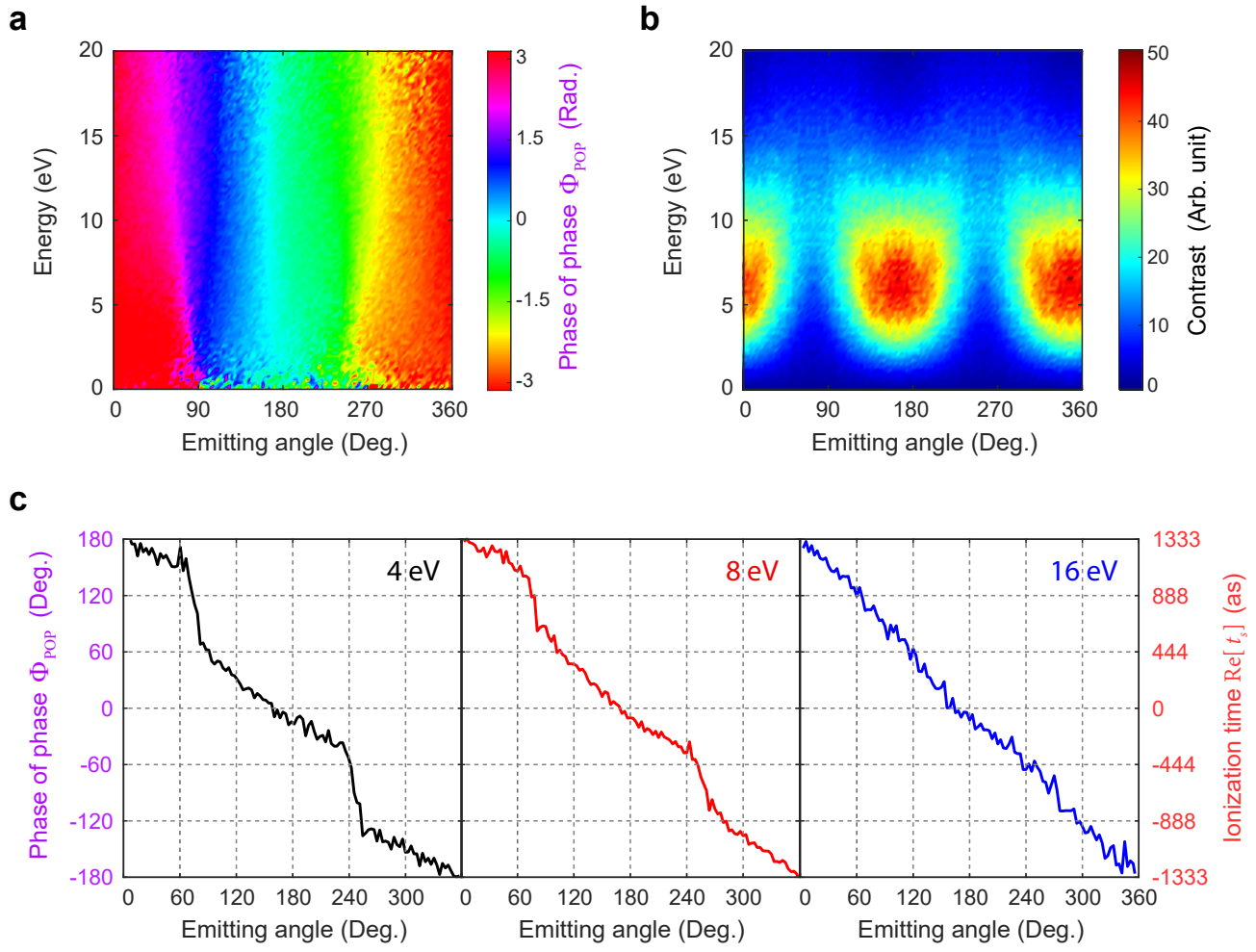

Figure 2: **Experimental results of the POP attoclock**. **a-b**, Measured phase-of-phase spectrum and contrast spectrum for krypton atoms in POP attoclock configuration, respectively. **c**, The cuts of Φ_{POP} along the energies of 4 eV, 8 eV and 16 eV. On the right vertical coordinate the phase of the phase is transformed to the ionization instant using $\Phi_{\mathrm{POP}} = \omega t$.

2a-b, respectively, which were obtained by Fourier transforming 72 frames of the angle-resolved photoelectron energy spectra with the resolution of $\Delta\phi_{\mathrm{RP}} = \pi/12$. Here we define the photoelectron emitting angle as $\theta = \arctan(p_z/p_x)$, and the momentum p_y along the laser propagation direction was integrated within [-0.1, 0.1] a.u. in the off-line data analysis. When the emitting angle varies 360 degrees, the phase of phase changes 2π radians or 360 degrees. This is equivalent to that the photoelectron emitting angle will rotate 360 degrees when varying the relative phase by 2π. More importantly, the slope of POP with respect to the photoelectron emitting angle reflects the electron rotation speed in the momentum plane. In Fig. 2c, we illustrate three cuts of the phase-of-phase spectrum along the energies of 4 eV, 8 eV and 16 eV, respectively, and convert Φ_{POP} to the ionization instant (see the right vertical coordinate of the plots). The results directly show the mapping relation between the emitting angle and the ionization instant is not angularly uniform, especially for the low-energy photoelectrons. The absolute value of the curve slope is less than 1 when θ ranges from 120° to 240° and from -60° to 60°, which indicates the electron rotates slowly when it arrives in the regions of the two main lobes (see Supplementary Section 3 for the animated photoelectron angular distribution). The mapping curve jumps quickly in the low-yield transitional zone between the two main lobes, where the FW clock hand points around the minor axis of the ellipse. For the high-energy electrons, their rotation speed is close to be isotropic. The POP spectrum intuitively shows a dynamical phenomenon that photoelectrons have a angle- and energy-dependent rotation speed even in a circular streaking field, which originates from the non uniform mapping relationship between the emitting angle and the ionization instant. The contrast spectrum is the extent of the response to the weak SH perturbation. Due to the perturbation is isotropic in POP attoclock, the contrast spectrum faithfully reflects the static photoelectron angle distribution in the elliptical FW.

To validate our observation and explanation, we first resort to two different tunneling models, the classical trajectory Monte-Carlo (CTMC) simulation[26–28] that is widely used for tunneling from a static barrier, and the strong-field approximation (SFA) model within the saddle-point approach[29] for the non-stationary tunneling. The previous attoclock experiments are mostly explained using the CTMC model[2,3,15]. In the CTMC model, there is neither electron sub-barrier dynamics nor the sub-barrier phase. The potential barrier shape is dictated by the instantaneous strength of the electric field adiabatically. At each ionization instant the tunneled electron burst has a Gaussian distribution centered at zero on the transverse momentum and has no any longitudinal momentum. Thus, the final momentum of the electron burst follows the opposite direction of the laser potential vector at the ionization instant with an additional Coulomb rotation angle. Finally, the photoelectron emission angle is linearly changed with respect to the ionization instant. In the CTMC simulation, we calculated a series of photoelectron momentum distributions at different relative phases and then extracted the phase of the phase with the same procedure for

experimental data. The obtained POP spectrum shows that the degree of linearity between the ionization instant and the emitting angle is pretty good (i.e., the slopes of the mapping curves in Fig. 3b are all close to -1). The left-right shift between these mapping curves can be attributed to the Coulomb rotation. In SI, we present the CTMC result without including the Coulomb potential and the obtained mapping curves are all overlapped. Thus, previous attoclok experiments that were interpreted with the CTMC model is not very accurate because the sub-barrrier effect is not seriously included.

By contrast, the non-stationary tunneling model (SFA) includes a time-dependent tunneling process on the imaginary time axis (see Fig. 4a). For the quantum path of each final momentum $\boldsymbol{p}$, its ionization time, i.e., the saddle point $t_s(\boldsymbol{p}) = t_r(\boldsymbol{p}) + t_i(\boldsymbol{p})$i, is a complex number governed by the saddle-point equation $[\boldsymbol{p} + \boldsymbol{A}(t_s)]^2/2 + I_p = 0$. The real part of the ionization time, t_r , represents the emitting instant from the barrier, which is the measured phase of the phase in this work. The imaginary part of the ionization time, t_i, is the so-called Keldysh tunneling time[30], which decides the duration time of the tunneling along the imaginary time axis. During the tunneling, i.e., progressing from t_s to t_r, the electron accumulates a time-dependent complex action $S[t_r(\boldsymbol{p})] = \int_{t_s}^{t_r} [\boldsymbol{p} + \boldsymbol{A}(t)]^2/2 + I_p \, dt$. The imaginary part of the action at the tunnel exit is associated with the probability of the quantum path by the exponential factor $\exp(-2\mathrm{Im}[\mathrm{S}])$, which corresponds to the measured contrast in POP attoclock. The real part of the action is the sub-barrier phase, which governs the initial phase of electron wave function in the continuum (see Fig. 4b). The laser field will excite the tunneling electron under the barrier and thus the quantum path model predicts a center-shifted Gaussian-like distribution for the transverse momentum and a nonzero time-dependent distribution for the longitudinal momentum at the exit[13,31,32]. These non-stationary tunneling features will destroy the uniform $\theta - t_r$ mapping relation in the CTMC model. In SI, we illustrate the time-resolved distributions of the exit velocities from SFA and use them as the initial condition for the CTMC simulation. The obtained POP spectrum emerges the non-uniform mapping. More discussions about the relation and difference between the static and the non-stationary tunneling models are presented in the theoretical part of Methods.

In Fig. 3c, we show the momentum-resolved distribution of t_r, which is obtained directly by solving the saddle-point equation *in the fundamental field*. The saddle-point result agrees with the experiment and the energy-dependent mapping relations between θ and t_r are well reproduced. Therefore, this POP-attoclock could reveal the features of the non-stationary tunneling, which are usually hidden in static photoelectron spectra of attoclock with one-color elliptically or circularly polarized fields. In Supplementary Figure 5, we present the extracted phase of phase spectrum using POP attoclock from calculated photoelectron momentum distributions by numerically integrating the transition matrix element of SFA, following the experimental and CTMC procedure. The extracted result

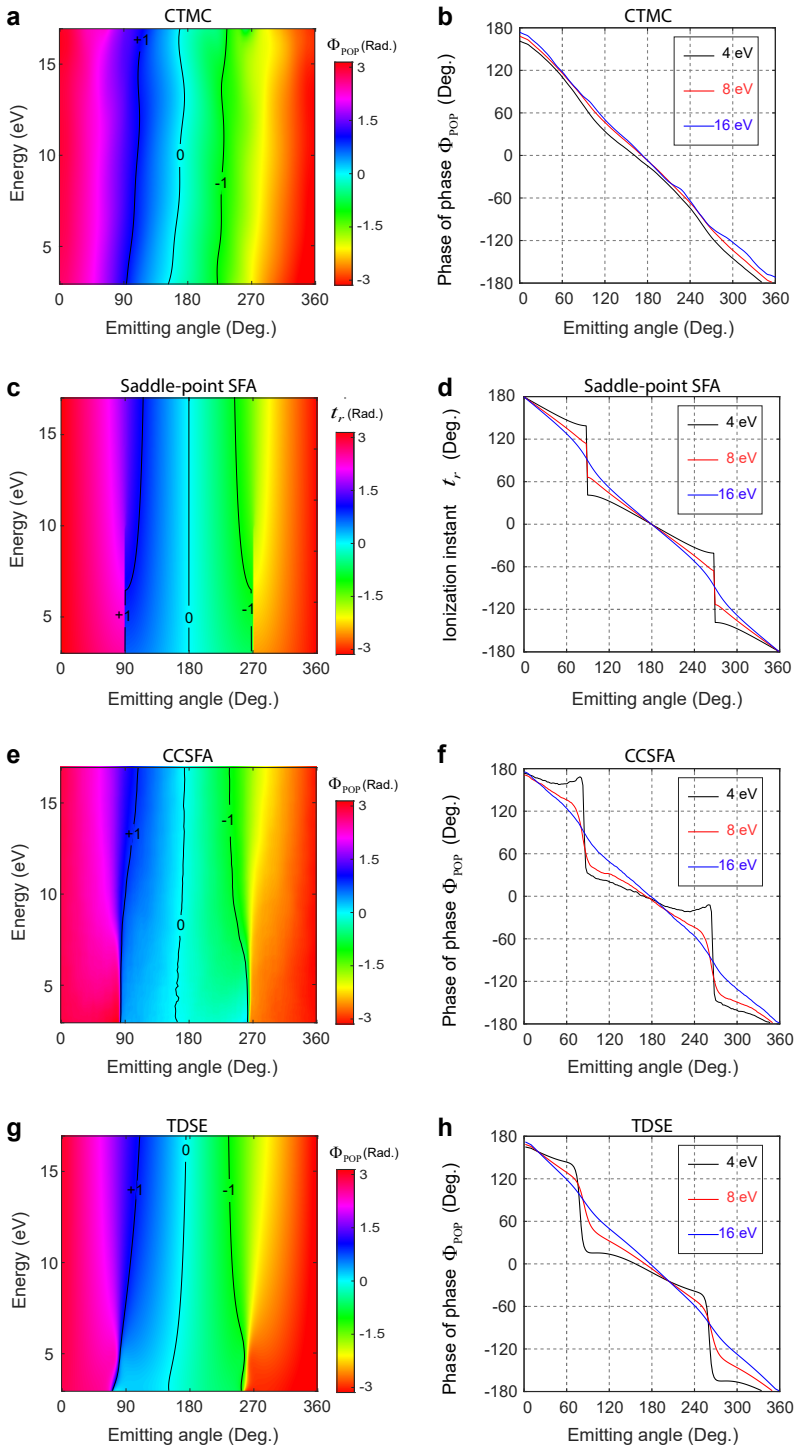

Figure 3: **Calculated phase-of-phase spectra**. **a,b**, The spectra of Φ_{POP} and the corresponding cuts along different energies from the CTMC simulation. **c,d**, The distribution of the real part of the saddle point and its corresponding cuts based on the SFA model. **e,f**, The results of the CCSFA simulation. **g,h**,The results of the TDSE simulation. The isolines of Φ_{POP} or t_r = 1.0, 0, and -1.0 radian are plotted in a,b,e, and g.

agrees very well with the saddle-point result, which self-consistently proves that the POP attoclock can measure the ionization instant. In circular or elliptical light fields, one needs to consider the influence of the magnetic quantum number of the ground state of atoms, since the p_+ and p_- orbitals will display the ionization dichroism in static photoelectron energy spectra[33,34]. The magnetic quantum number will affect the probability of electron trajectories via the pre-exponential factor of the transition matrix element but has no effect on the saddle point. Therefore, the POP spectrum is less sensitive to the magnetic quantum number, and on the contrary the contrast spectrum will show the same ionization dichroism features as the static photoelectron energy spectrum (see Supplementary Figure 4). To reveal the dependence of the POP spectrum on the nonadiabaticity of tunneling, in Supplementary Figure 6 we present the calculated POP spectra at other two wavelengths (1200 nm and 1800 nm) for the FW from the SFA model. The result demonstrates that the non-uniform mapping gradually disappears with the increase of laser wavelength or the nonadiabaticity of tunneling.

In all attoclock experiments, the rotation of the long-range Coulomb potential by elliptical or circular fields will modify the electron momentum after tunneling, and mainly causes the offset angle in the final momentum plane. To investigate the effect of the Coulomb potential on the POP spectrum, we have further performed the calculation with the Coulomb-corrected strong-field model[35–37] (CCSFA) and the numerical solution of the time-dependent Schrödinger equation[38] (TDSE) (see Methods for the details). The CCSFA model is based on SFA and the effect of the long-range Coulomb potential has been included. The TDSE results can be viewed as the benchmark for all the models. From the results of these two models, the POP spectrum will be shift by the offset angle, as indicated by the ioslines in Fig. 3e-g. Both models show the low-energy electrons will be more affected by the Coulomb rotation. Although the Coulomb rotation will shift the POP spectrum left to some extent, basically it does not alter the slope of the POP curves (see the CTMC result in Fig. 3a-b), which reflects the sub-barrier non-stationary tunneling dynamics.

Importantly, the tunneling process not only modifies the amplitude of the electron wavepacket (i.e., initial momentum distributions), but also imprints a remarkable phase on it. The POP attoclock enables us to obtain the electron sub-barrier phase information. This approach does not need the interference pattern on photoelectron momentum distribution[39]. With the measured phase of the phase and the contrast, we can further reconstruct the other two quantities of the imaginary-time tunneling picture, t_i and Re[S], according to the sub-barrier integration equation of the action. Our reconstruction approach is very straightforward and robust, which has been justified using the input of t_r and Im[S] extracted from the photoelectron momentum spectra of SFA (see Supplementary Figure 5). To isolate the sub-barrier dynamics from the classical dynamics in the continuum, one needs to subtract the Coulomb rotation angle from the measured photoelectron emission angle, being consistent with the SFA model.

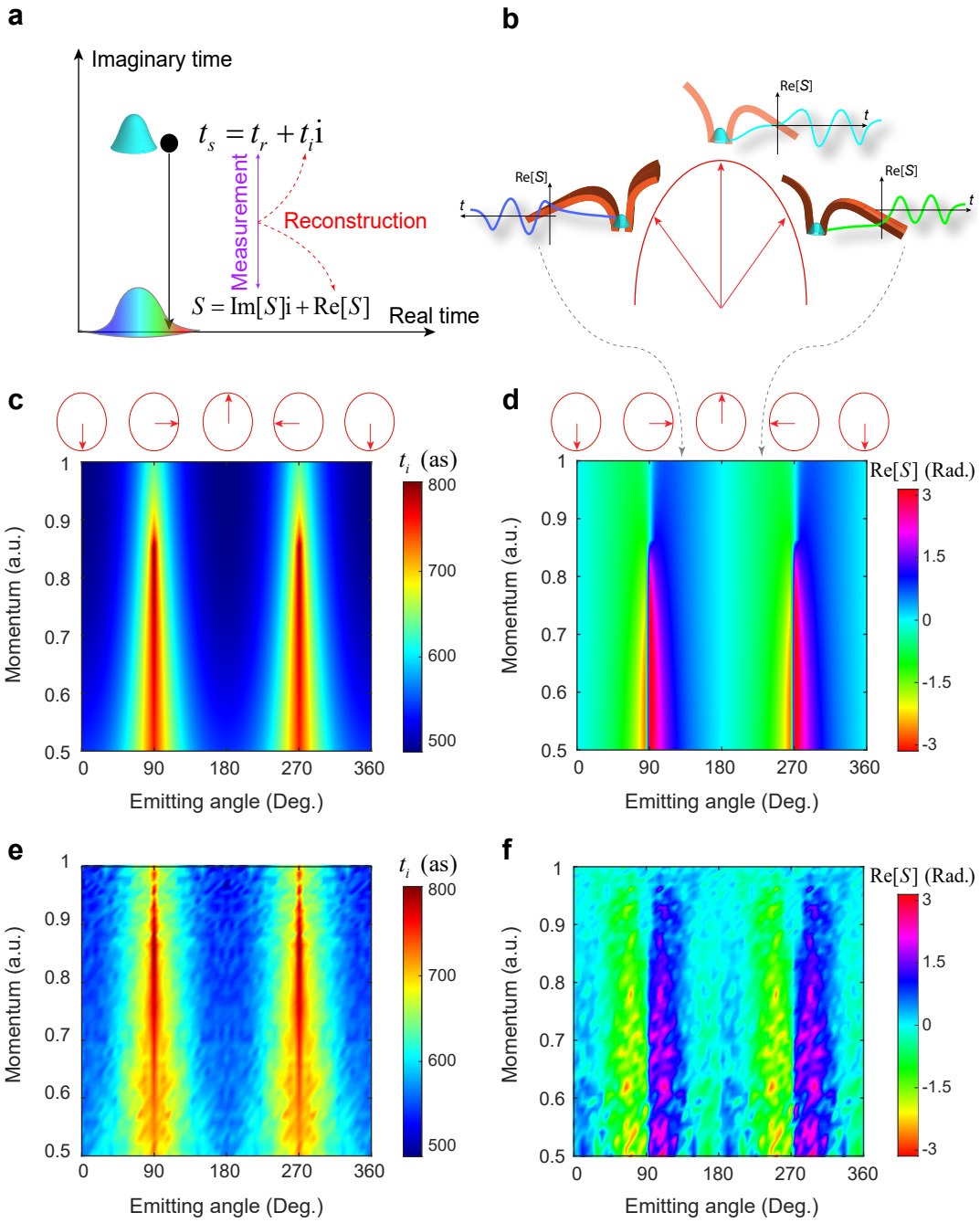

Figure 4: **Sub-barrier tunneling dynamics.** **a**, Tunneling picture and the reconstruction of t_i and Re[S]. **b**, Illustrations for the phase evolution at three ionization instants. The sub-barrier phase indicated by Re[S] at the tunnel exit, is dependent on the dynamical change of the barrier. **c-d**, The final-momentum-resolved distribution of the imaginary tunneling time t_i and the sub-barrier phase Re[S], respectively, which are obtained by solving the saddle-point equation and the integration equation of the action. **e-f**, The reconstructed distributions of t_i and Re[S] using the measured phase-of-phase spectrum and the contrast spectrum, respectively.

The reconstructed results from experiments (Fig. 4e-f) agree well with the theoretical results of the quantum path approach (Fig. 4c-d), revealing a clear time- and energy-dependent sub-barrier feature on the distributions.

For the imaginary tunneling time t_i, it reflects the static property of the potential barrier, i.e., the barrier thickness decided by the instantaneous strength of the electric field. The imaginary tunneling time will reach the minimum ($\sim$ 500 attoseconds) when the electric field vector points to the major axis of the ellipse (i.e., the emitting angle $\theta = 180^\circ$) and it will increase to 800 attoseconds when the polarization vector points to the minor axis. The energy dependence of t_i is also important, which controls the radial spread of the photoelectron momentum distribution. Under the adiabatic approximation [$E(t) = E$, $A(t) = -Et$], the imaginary tunneling time can be obtained analytically as $t_i = \sqrt{(2I_p)}/E$, and it has no any energy dependence. The corresponding ionization rate $\exp(-2\mathrm{ImS})$ becomes back to the ADK rate[40] used in CTMC (i.e., $\exp[-2(2I_p)^{3/2}/(3E)]$), which shows a narrower radial spread of the photoelectron momentum distribution compared with the non-adiabatic case[13,14].

In contrast to the imaginary tunneling time, the sub-barrier phase reflects the dynamical properties of the quickly changing Coulomb barrier, i.e, the derivative versus time. When the electric field vector points to the major or minor axis of the ellipse, the barrier is stationary and thus the electron doesn't acquire any phase in agreement with the Wentzel–Kramers–Brillouin approximation solution (real number) under the barrier[41]. When the electric field vector deviates the stationary instants, the electron acquires a sub-barrier phase whose sign is dependent on the change direction of the barrier, i.e., the barrier thickness is increasing or decreasing. In Fig. 4b, we illustrate the phase evolution at three ionization instants at the rising edge, stationary point, and falling edge of the light electric field, respectively. This clearly proves the sub-barrier phase is dependent on the dynamical change of the barrier. Moreover, both experiment and theory indicate that the low-energy component of the tunneling wave function has a more prominent sub-barrier phase, as there the sub-barrier interaction time and length are larger. Note that the POP attoclock can provide the time- and energy-resolved dynamical information about tunneling compared with the common static attoclock scheme.

In conclusion, we have calibrated the attoclock with the two-color phase-of-phase photoelectron spectroscopy, and employed this POP attoclock to build the accurate angular streaking relationship between an arbitrary final momentum and its ionization instant in the full momentum space. The results demonstrate the widely-used angular streaking capability of light fields is not angularly homogeneous and the ionization instants along the same emitting angle have a strong energy dependence, which both contradict with the static tunneling model. Using the measured ionization instant and ionization probability, we have reconstructed the imaginary tunneling time and the electron sub-barrier phase, which contains the static and dynamical information of the tunneling process, serving as a

complete characterization of sub-barrier tunneling dynamics in strong-field ionization. Based on this work, the POP attoclock has the appealing potential application in the attosecond metrology of the oriented molecules, crystal solids and liquids[42].

Methods

Experimental details. Supplementary figure 1 schematically shows the experimental setup for phase-of-phase attoclock. The p-polarization fundamental light field pulses were delivered from a multipass Ti:sapphire amplifier at a central wavelength of 800 nm with the repetition rate of 3 kHz. The pulse duration is 25 fs with full width of half maximum in intensity. The second harmonic pulses at the central wavelength of 400 nm were produced by frequency doubling with a 200-μm-thick type-I beta-barium borate (BBO) crystal (29.2° cut). Then, the two light fields were synchronized in a Mach-Zehnder interferometer scheme with 5-attosecond precision and their polarizations and intensities were controlled, independently. In each arm of the interferometer, the intensity and polarization of the light field were monitored by a wire grid polarizer and half-wave and quarter-wave retardation plates, respectively. The fundamental field was adjusted to be the elliptical polarization whose major axis was fixed along the z axis and the second harmonic field was tuned to a co-rotating circular polarization in the same polarization plane (x-z plane). The light beam was focused by a silver-coated concave mirror with focal length f = 75 mm, which was placed inside the high-vacuum chamber ($< 10^{-10}$ mbar) of the COLTRIMS set-up. The supersonic gas jet of krypton atoms (2 Bar) was delivered along the x direction by a small nozzle with a opening hole diameter of 30 μm. In COLTRIMS, static electric ($\sim$ 3.2 V/cm) and magnetic ($\sim$ 5.4 G) fields were applied along the z axis to collect the charged fragments in coincidence. Only the single ionization (one electron is coincident with one kr^+) events are presented in this work.

CTMC simulation. In the CTMC model,the tunnelled electrons have a Gaussian distribution on the transverse momentum ($v_\perp$) perpendicular to the instantaneous laser field and zero longitudinal momentum along the instantaneous laser field direction. Each electron trajectory is weighted by the ADK ionization rate $W(t, v_\perp^i) = W_0(t)W_1(v_\perp^i)$[27,28], in which $W_0(t) = |(2I_p)^2/E(t)|^{2/\sqrt{2I_p}-1}\exp[-2(2I_p)^{3/2}/|3E(t)|]$ determines the ionization rate with respect to the ionization instant, and $W_1(v_\perp^i) = \sqrt{2I_p}/E(t)\exp[-\sqrt{2I_p}(v_\perp^i)^2/|E(t)|]$ determines the initial transverse momentum distribution, where $E(t)$ is the instantaneous strength of laser field and I_p is the ionization potential. The electron tunneling exit is along the instantaneous direction of the synthesized light field and its value is given by $I_p/|E(t)|$. After sampling all the electrons, their classical motion outside the barrier is governed by the Newtonian equation $\ddot{\mathbf{r}} = -E(t) - \mathbf{r}/r^3$ until the laser is turned off, where r is the distance from the electron to the nucleus. In the simulation, we use a $\sin^2$-shape pulse envelope with the duration of 12 cycles for the SH field. At the end of the

laser pulse, we select the electrons with positive energy and record their positions and their momenta. The electron asymptotic momenta on the virtual detector are transformed according to the Kepler's laws. Finally, we statistic the electron trajectories using the 200×200 bins in the momentum regime of $p_x \times p_z$= [-1.5,1.5]a.u.×[-1.5,1.5]a.u.. We totally calculate 24 frames of the photoelectron momentum distributions for the two-color relative phase distributing from 0 to 2π uniformly. The calculated phase-resolved photoelectron momentum distributions are presented in SI, from which we use Fourier transform to obtain the phase-of-phase spectrum shown in Fig. 3a.

Strong-field approximation model. In the strong-field approximation, the final-momentum-resolved ionization matrix element is given by $M_{\boldsymbol{p}} = -\mathrm{i}\int_0^{\mathrm{t_f}} <\boldsymbol{p}+\boldsymbol{A}(\tau)|\boldsymbol{r}\cdot\boldsymbol{E}(\tau)|\psi_{\mathrm{initial}}> \exp(\mathrm{i}S(\tau))d\tau$, where $S(\tau) = \int_0^{\tau}[\boldsymbol{p}+\boldsymbol{A}(t)]^2/2 + I_p dt$, t_f is the laser turn-off time, and ψ_{initial} is the initial wavefunction of electrons. In the calculation,we adopt the asymptotic form of the hydrogenlike atomic wavefunction $\psi_{\mathrm{initial}} = \exp(-\sqrt{(}2\mathrm{I_p})r)\mathrm{Y}_{1m}(\theta,\phi)/r$ as the initial wavefuntion of Kr atoms, where $m = 1$ and -1 represent the p_+ and p_- orbitals, respectively. By the numerically integrating the ionization matrix element, we obtained the phase-resolved photoelectron momentum distributions from p_+ and p_- orbitals, respectively. From the photoelectron momentum spectra, we extracted the phase-of-phase spectrum. Note that using the saddle-point method one can avoid the numerical integration and introduce the concept of the quantum path. The saddle point $t_s(\boldsymbol{p})$ is determined by the equation $[\boldsymbol{p}+\boldsymbol{A}(t_s)]^2/2 + I_p = 0$, which is solved by a complex root finding routine. In the elliptical light field, one final momentum can correspond to two saddle points and only one of them is physical. By judging the ionization probability of the quantum path, one can select the physical one. During tunneling (i.e., from t_s to t_r), the electron acquires a complex action $S(t_r) = \int_{t_s}^{t_r}[\boldsymbol{p}+\boldsymbol{A}(\tau)]^2/2 + I_p d\tau$. The real part of the action is the sub-barrier phase and the imaginary part governs the ionization rate by $W = \exp(-2\mathrm{Im}[S(t_r)])$. In the main text, we show t_r, t_i and $\mathrm{Re}[S]$, which are obtained by directly solving the saddle-point equation and propagates the quantum path under the barrier. On the other hand, we present the corresponding results in SI, which are obtained by the extraction method of POP attoclock. They agree very well with each other, which strongly verified the reliability of POP attoclock. Note that in the adiabatic limit $[E(t) = E, A(t) = -Et]$, there is $t_i = \sqrt{(}v_\perp + 2I_p)/E$ and thus the exponential factor of the ionization rate can be evaluated as $W = \exp[-2(2I_p)^{3/2}/(3E)]\exp[-\sqrt{2\mathrm{I_p}}(v_\perp)^2/E]$, which is exactly the ADK rate used in the adiabatic CTMC model.

Coulomb-corrected strong-field approximation simulation. The CCSFA model is based on the saddle-point approach of the SFA. We randomly sample 10^7 points in the final momentum plane ($p_x,\ p_z = [-1.5, 1.5]$ a.u.). After determining the ionization time of each quantum path by the saddle-point equation in the two-color field, we then propagate these electron trajectories with real variables using Newton's equation $\ddot{\mathbf{r}} = -E(t) - \mathbf{r}/r^3$ to simulate the

electron dynamics outside the barrier. The weight of the electron trajectories is given by $W = \exp(-2\mathrm{Im}[S(t_r)])$ without considering the pre-exponential factor. The electron tunnel exit position and exit momentum are determined by the imaginary-time propagation under the barrier, i.e., $\boldsymbol{r}_{exit} = \int_{t_s}^{t_r}[\boldsymbol{p}+\boldsymbol{A}(t)]dt$ and $\boldsymbol{p}_{exit} = \boldsymbol{p}+\boldsymbol{A}(t_r)$. After the laser pulse turns off, we obtain the electron asymptotic momenta on the virtual detector according to the Kepler's laws. Then we obtain the photoelectron momentum distribution on the "detector" using the same method as CTMC.

TDSE simulation. Details of the algorithm and the source code are in the publication[38]. Briefly, we first obtain the atomic initial-state wave-function through the imaginary time propagation method. In the simulation we use the effective model potential $V_{eff} = -[Z + (Z_{full} - Z)\exp(-r_s \cdot r)]/r$, where $Z = 1$ and $Z_{full} = 36$ are the asymptotic ion charges as $r \to \infty$ and $r \to 0$, respectively. The screening length $r_s = 7.7631$ is used to match the ionization potential $I_p = -14.0$ eV for krypton atom. The initial magnetic quantum number m can be tuned to 1, 0 and -1 without changing the ionization potential. The laser parameters are identical in all simulations shown in the main text. Secondly, we perform the real-time evolution of the wave-function in the laser and the Coulomb combined field within the dipole approximation. The wave-function is expanded in spherical harmonics, and time-propagation is performed using a split-operator approach. Finally, when the laser turns off, the photoelectron momentum distribution is evaluated with a time-dependent surface flux method. The calculated phase-resolved movie of photoelectron momentum distributions is shown in SI. From these photoelectron momentum distributions we extract the POP spectrum shown in Fig. 3g.

Reconstruction of t_i and Im[S]. Using the expression of the laser field, one can derive the real part and imaginary part of the electron sub-barrier action analytically, as given by,

$$\begin{aligned}\mathrm{Re[S]} =& -p_z E_\omega/\omega^2 \cos\omega t_r(1-\cosh\omega t_i) - p_x \varepsilon E_\omega/\omega^2 \sin\omega t_r(1-\cosh\omega t_i)\\ &+(1-\varepsilon^2)E_\omega^2/(8\omega^3)\sin 2\omega t_r(1-\cosh 2\omega t_i).\end{aligned} \tag{1}$$

$$\begin{aligned}\mathrm{Im[S]} =& (p^2/2 + I_p + U_p)t_i - p_z E_\omega/\omega^2 \sin\omega t_r \sinh\omega t_i\\ &+ p_x \varepsilon E_\omega/\omega^2 \cos\omega t_r \sinh\omega t_i - (1-\varepsilon^2)E_\omega^2/(8\omega^3)\cos 2\omega t_r(\sinh 2\omega t_i).\end{aligned} \tag{2}$$

The phase-of-phase spectrum directly reflects the distribution of t_r, and the contrast spectrum is corresponding to $\exp(-2\mathrm{Im[S]})$, which is normalized to the maximum of the theoretical distribution in the reconstruction process. Using the measured spectra of t_r and $\exp(-2\mathrm{Im[S]})$, we start from Equation 2 to evaluate t_i by the numerical method of solving the non-linear equation for each final momentum. Then using the measured t_r and the reconstructed t_i,

through Equation 1 we can obtain Re[S], i.e., the sub-barrier phase. Note that we have reduced the classical Coulomb rotating effect in experiment. The electron emitting angle θ was shifted to cancel the offset angle in reconstruction process, which is in consistence with the SFA model.

Data availability

The data that support the plots within this paper and other findings of this study are available from the corresponding author upon reasonable request.

References

1. Corkum, P. B. & Krausz, F. Attosecond science. *Nat. Phys.* **3**, 381–387, DOI: 10.1038/nphys620 (2007).
2. Eckle, P. *et al.* Attosecond angular streaking. *Nat. Phys.* **4**, 565–570, DOI: 10.1038/nphys982 (2008).
3. Eckle, P. *et al.* Attosecond ionization and tunneling delay time measurements in helium. *Science* **322**, 1525–1529, DOI: 10.1126/science.1163439 (2008).
4. Torlina, L. *et al.* Interpreting attoclock measurements of tunnelling times. *Nat. Phys.* **11**, 503–508, DOI: 10.1038/nphys3340 (2015).
5. Sainadh, U. S. *et al.* Attosecond angular streaking and tunnelling time in atomic hydrogen. *Nature* **568**, 75–77, DOI: 10.1038/s41586-019-1028-3 (2019).
6. Camus, N. *et al.* Experimental Evidence for Quantum Tunneling Time. *Phys. Rev. Lett.* **119**, 023201, DOI: 10.1103/PhysRevLett.119.023201 (2017).
7. Ni, H., Saalmann, U. & Rost, J.-M. Tunneling Ionization Time Resolved by Backpropagation. *Phys. Rev. Lett.* **117**, 023002, DOI: 10.1103/PhysRevLett.117.023002 (2016).
8. Yakaboylu, E., Klaiber, M. & Hatsagortsyan, K. Z. Wigner time delay for tunneling ionization via the electron propagator. *Phys. Rev. A* **90**, 012116, DOI: 10.1103/PhysRevA.90.012116 (2014).
9. Teeny, N., Yakaboylu, E., Bauke, H. & Keitel, C. H. Ionization Time and Exit Momentum in Strong-Field Tunnel Ionization. *Phys. Rev. Lett.* **116**, 063003, DOI: 10.1103/PhysRevLett.116.063003 (2016).
10. Han, M. *et al.* Unifying Tunneling Pictures of Strong-Field Ionization with an Improved Attoclock. *Phys. Rev. Lett.* **123**, 073201, DOI: 10.1103/PhysRevLett.123.073201 (2019).
11. Eicke, N., Brennecke, S. & Lein, M. Attosecond-Scale Streaking Methods for Strong-Field Ionization by Tailored Fields. *Phys. Rev. Lett.* **124**, 43202, DOI: 10.1103/PhysRevLett.124.043202 (2020).

12. Pedatzur, O. *et al.* Attosecond tunnelling interferometry. *Nat. Phys.* **11**, 815–819, DOI: 10.1038/nphys3436 (2015).

13. Li, M. *et al.* Experimental verification of the nonadiabatic effect in strong-field ionization with elliptical polarization. *Phys. Rev. A* **95**, 053425, DOI: 10.1103/PhysRevA.95.053425 (2017).

14. Eckart, S. *et al.* Direct Experimental Access to the Nonadiabatic Initial Momentum Offset upon Tunnel Ionization. *Phys. Rev. Lett.* **121**, 163202, DOI: 10.1103/PhysRevLett.121.163202 (2018).

15. Pfeiffer, A. N. *et al.* Attoclock reveals natural coordinates of the laser-induced tunnelling current flow in atoms. *Nat. Phys.* **8**, 76–80, DOI: 10.1038/nphys2125 (2012).

16. Han, M. *et al.* Revealing the Sub-Barrier Phase using a Spatiotemporal Interferometer with Orthogonal Two-Color Laser Fields of Comparable Intensity. *Phys. Rev. Lett.* **119**, DOI: 10.1103/PhysRevLett.119.073201 (2017).

17. Ni, H., Saalmann, U. & Rost, J.-M. Tunneling exit characteristics from classical backpropagation of an ionized electron wave packet. *Phys. Rev. A* **97**, 013426, DOI: 10.1103/PhysRevA.97.013426 (2018).

18. Skruszewicz, S. *et al.* Two-Color Strong-Field Photoelectron Spectroscopy and the Phase of the Phase. *Phys. Rev. Lett.* **115**, 043001, DOI: 10.1103/PhysRevLett.115.043001 (2015).

19. Almajid, M. A., Zabel, M., Skruszewicz, S., Tiggesbäumker, J. & Bauer, D. Two-color phase-of-the-phase spectroscopy in the multiphoton regime. *J. Phys. B: At. Mol. Opt. Phys.* **50**, 194001, DOI: 10.1088/1361-6455/aa896a (2017).

20. Braß, J., Milbradt, R., Villalba-Chávez, S., Paulus, G. G. & Müller, C. Two-color phase-of-the-phase spectroscopy applied to nonperturbative electron-positron pair production in strong oscillating electric fields. *Phys. Rev. A* DOI: 10.1103/PhysRevA.101.043401 (2020).

21. Tulsky, V. A., Almajid, M. A. & Bauer, D. Two-color phase-of-the-phase spectroscopy with circularly polarized laser pulses. *Phys. Rev. A* **98**, 053433, DOI: 10.1103/PhysRevA.98.053433 (2018).

22. Würzler, D. *et al.* Accurate retrieval of ionization times by means of the phase-of-the-phase spectroscopy, and its limits. *Phys. Rev. A* **101**, 033416, DOI: 10.1103/PhysRevA.101.033416 (2020).

23. Tulsky, V. A., Krebs, B., Tiggesbäumker, J. & Bauer, D. Revealing laser-coherent electron features using phase-of-the-phase spectroscopy. *J. Phys. B: At. Mol. Opt. Phys.* **53**, 074001, DOI: 10.1088/1361-6455/ab69ab (2020).

24. Dörner, R. *et al.* Cold Target Recoil Ion Momentum Spectroscopy: a 'momentum microscope' to view atomic collision dynamics. *Phys. Reports* **330**, 95–192, DOI: 10.1016/S0370-1573(99)00109-X (2000).

25. Ullrich, J. *et al.* Recoil-ion and electron momentum spectroscopy: reaction-microscopes. *Reports on Prog. Phys.* **66**, 1463–1545, DOI: 10.1088/0034-4885/66/9/203 (2003).

26. HuP, B., Liu, J. & Chen, S.-g. Plateau in above-threshold-ionization spectra and chaotic behavior in rescattering processes. *Phys. Lett. A* **236**, 533–542, DOI: 10.1016/S0375-9601(97)00811-6 (1997).

27. Li, M. *et al.* Subcycle Dynamics of Coulomb Asymmetry in Strong Elliptical Laser Fields. *Phys. Rev. Lett.* **111**, 023006, DOI: 10.1103/PhysRevLett.111.023006 (2013).

28. Sun, X. *et al.* Calibration of the initial longitudinal momentum spread of tunneling ionization. *Phys. Rev. A - At. Mol. Opt. Phys.* **89**, 45402, DOI: 10.1103/PhysRevA.89.045402 (2014).

29. Milošević, D. B., Paulus, G. G., Bauer, D. & Becker, W. Above-threshold ionization by few-cycle pulses. *J. Phys. B: At. Mol. Opt. Phys.* **39**, R203–R262, DOI: 10.1088/0953-4075/39/14/R01 (2006).

30. V Popruzhenko, S. Keldysh theory of strong field ionization: history, applications, difficulties and perspectives. *J. Phys. B: At. Mol. Opt. Phys.* **47**, 204001, DOI: 10.1088/0953-4075/47/20/204001 (2014).

31. Geng, J.-W. *et al.* Nonadiabatic tunneling ionization of atoms in elliptically polarized laser fields. *J. Phys. B: At. Mol. Opt. Phys.* **47**, 204027, DOI: 10.1088/0953-4075/47/20/204027 (2014).

32. Han, M., Li, M., Liu, M.-M. & Liu, Y. Tunneling wave packets of atoms from intense elliptically polarized fields in natural geometry. *Phys. Rev. A* **95**, 023406, DOI: 10.1103/PhysRevA.95.023406 (2017).

33. Barth, I. & Smirnova, O. Nonadiabatic tunneling in circularly polarized laser fields: Physical picture and calculations. *Phys. Rev. A* **84**, DOI: 10.1103/PhysRevA.84.063415 (2011).

34. Eckart, S. *et al.* Ultrafast preparation and detection of ring currents in single atoms. *Nat. Phys.* DOI: 10.1038/s41567-018-0080-5 (2018). 1802.06630.

35. Popruzhenko, S. V. & Bauer, D. Strong field approximation for systems with Coulomb interaction. *J. Mod. Opt.* **55**, 2573 (2008).

36. Yan, T.-M., Popruzhenko, S. V., Vrakking, M. J. J. & Bauer, D. Low-Energy Structures in Strong Field Ionization Revealed by Quantum Orbits. *Phys. Rev. Lett.* **105**, 253002 (2010).

37. Huismans, Y. *et al.* Time-resolved holography with photoelectrons. *Science* **331**, 61–64, DOI: 10.1126/science.1198450 (2011).

390 **38.** Mosert, V. & Bauer, D. Photoelectron spectra with qprop and t-surff. *Comput. Phys. Commun.* **207**, 452–463,
391 DOI: https://doi.org/10.1016/j.cpc.2016.06.015 (2016).

392 **39.** Han, M., Ge, P., Shao, Y., Gong, Q. & Liu, Y. Attoclock Photoelectron Interferometry with Two-Color
393 Corotating Circular Fields to Probe the Phase and the Amplitude of Emitting Wave Packets. *Phys. Rev. Lett.*
394 **120**, 073202, DOI: 10.1103/PhysRevLett.120.073202 (2018).

395 **40.** Ivanov, M. Y., Spanner, M. & Smirnova, O. Anatomy of strong field ionization. *J. Mod. Opt.* **52**, 165–184, DOI:
396 10.1080/0950034042000275360 (2005).

397 **41.** Landau, L. D. & Lifschitz, E. M. *Quantum Mechanics (Non-relativistic Theory)* (Oxford Univ. Press, New York,
398 1958).

399 **42.** Jordan, I. *et al.* Attosecond spectroscopy of liquid water. *Science* DOI: 10.1126/science.abb0979 (2020).

400 Acknowledgements

401 Y. L. acknowledges the finance support by the National Science Foundation of China (grant numbers: 92050201,
402 918850111, 11774013). M. H. acknowledges funding from the European Union's Horizon 2020 research and
403 innovation programme under the Marie Skłodowska-Curie grant agreement No 801459 - FP-RESOMUS - and the
404 Swiss National Science Foundation through the NCCR MUST.

405 Author contributions statement

406 M. H., P. G., and Z. G. performed the experiments. M. H., Y. F. and Y. L. analyzed and interpreted the data.
407 Simulations were implemented by M. H.. This project was coordinated by Y. L.. All authors discussed the results
408 and wrote the paper.

409 Competing interests

410 The authors declare no competing interests

411 Additional information

412 Supplementary information is available for this paper. Correspondence and requests for materials should be addressed
413 to Y. L..